metals

MDPI

Article

Use of the Critical Acidification Model to Estimate the Influence of W in the Localized Corrosion Resistance of 25Cr Super Duplex Stainless Steels

Cristian Torres [1,*], Mariano Iannuzzi [1,2] and Roy Johnsen [1]

[1] Department of Mechanical and Industrial Engineering, Norwegian University of Science and Technology, Richard Birkelands veg 2b, 7491 Trondheim, Norway; mariano.iannuzzi@curtin.edu.au (M.I.); roy.johnsen@ntnu.no (R.J.)

[2] Curtin Corrosion Centre, Curtin University, GPO Box U1987, Perth, WA 6845, Australia

* Correspondence: cristian.torres@ntnu.no; Tel.: +47-7359-3761

Received: 6 August 2020; Accepted: 4 October 2020; Published: 13 October 2020

Abstract: Two super duplex stainless steels (SDSS) with different W content, namely UNS S32750 (W-free) and UNS S39274 (2.1 wt.% W), were tested in simulated crevice corrosion environments to determine the influence of W on their corrosion resistance. Anodic potentiodynamic polarization experiments were performed in two different crevice-like-solutions: 1 M HCl (as reference for a pH = 0 environment), and 7 M LiCl, adjusted to the same pH value. Galvele's critical acidification model was used to estimate the theoretical critical potential (E_{crit}) and comparatively evaluate the corrosion resistance of the two SDSS. The anodic potentiodynamic polarization results showed a statistically significant difference between the two materials in only one test condition, i.e., 7 M Cl^- at 60 °C. Additionally, the quantification of chemical dissolution of the metal cations after the tests suggested a surface enrichment in W only in the 7 M chloride solution. Scanning electron microscope (SEM) analysis indicated a uniform dissolution experienced by UNS S32750 in this environment, whereas UNS S39274 suffered selective corrosion of the ferrite-phase. These observations were reflected in a slight increase in the E_{crit} values of UNS S32974 estimated with Galvele's model.

Keywords: acidification model; tungsten; crevice-like-solutions; super duplex stainless steel

1. Introduction

Super duplex stainless steels (SDSS) have excellent corrosion resistance in neutral chloride-containing environments thanks to their high content of alloying elements such as Cr, Mo, and N [1–4]. Tungsten (W) is another element that has been shown to improve corrosion resistance. However, the effect of W on localized corrosion resistance is still disputed, as discussed in detail elsewhere [5,6].

A recent publication reviewed and studied the influence of W additions to SDSS on the precipitation kinetics of tertiary phases. In this regard, tertiary phases such as σ- and χ-phase are well known to be deleterious to both mechanical properties and corrosion resistance [5]. The authors showed that about 2 wt.% W reduced the total concentration of deleterious phases, and retarded the precipitation of σ-phase, favoring the formation of χ-phase at grain and phase boundaries. When W was added at approximately 0.6 wt.%, W promoted deleterious phase precipitation and impacted the localized corrosion resistance of the material negatively.

Another recent publication [6] examined the influence of W as a solid solution element, i.e., in the absence of tertiary phases, on the crevice corrosion resistance of the same SDSS. The authors compared the critical crevice repassivation temperature ($T_{R,Crev}$) obtained by the potentiodynamic-galvanostatic-potentiodynamic (PD-GS-PD) technique with critical crevice

temperature (CCT) and $T_{R,Crev}$ values from long-term exposure in natural seawater. The results showed that both the CCT and $T_{R,Crev}$ increased with W content, with a difference of up to 10 °C between the W-free and 2.1 wt.% W cases, depending on the test conditions.

Despite quantifying the influence of W on localized corrosion resistance in neutral chloride environments and natural seawater, little is known about the mechanisms by which W influences corrosion resistance. It was, thus, desirable to investigate the performance of commercial SDSS in simulated crevice solutions, as done by Galvele [7], Newman [8], and others [9–12] for various alloys.

Crevice-Like-Solutions and the Critical Acidification Model

Investigations in simulated pit/crevice environments can provide information about the role of alloying elements on the localized corrosion resistance of the materials, as first suggested by Galvele's critical acidification model [13] described in Equation (1).

$$E_{crit} = E_{corr}{}^{*} + \eta + \phi + E_{inh}. \quad (1)$$

In Equation (1), $E_{corr}{}^{*}$ is the corrosion potential of the material in the simulated pit or crevice electrolyte, η is the anodic polarization (overpotential) required to sustain an i_{crit} value at the bottom of the pit or crevice, ϕ is the ohmic potential drop along the pit or crevice, and E_{inh} is an additional polarization required in the presence of buffers or inhibitors. The critical potential (E_{crit}) is the theoretical pitting/crevice potential in a neutral chloride environment, obtained from measurements in the simulated acidic pit or crevice electrolyte [7].

Even though Galvele developed the critical acidification model for pure metals, the approach has been used for engineering alloys such as stainless steels and nickel-based alloys [7,10,11,14,15]. Galvele et al. [7] applied the critical acidification model to investigate the effect of Mo content in ferritic stainless steels (18Cr). Mo was found to decrease dissolution kinetics, changing the rate of pit propagation. Bocher et al. [14] investigated the influence of Mo additions to Ni-alloys using Galvele's model in two different crevice-like-solutions, i.e., localized environment inside a corroding crevice. The model was able to distinguish the performance of the same material (alloy 625) in two different product forms (plate and wire), even though their pitting resistance equivalent (PRE_N) was identical. Therefore, these authors concluded that the critical acidification model could be used to distinguish the influence of minor alloying elements on localized corrosion performance.

Srinivasan et al. [15] provided a detailed overview of Galvele's critical acidification model and the artificial 1D pit method, quantifying, among others, the minimum pH at which a protective oxide would precipitate. This critical minimum pH defined the repassivation of the active attack, i.e., pitting corrosion repassivation occurs when the critical metallic cation concentration and pH inside the pit/crevice stop being sustainable. Hornus et al. [10] measured the crevice repassivation potential ($E_{R,Crev}$) of two stainless steels (UNS S30400 and UNS S31600) and compared the difference in localized corrosion resistance using Galvele's model. By equating $E_{R,Crev}$ values measured with the PD-GS-PD technique to Equation (1), the authors concluded that the effect of a 2.5 wt.% Mo addition was related mainly to the ohmic potential drop (ϕ) term.

A detailed review of different solutions used to simulate active pits and crevices has been reported by Kappes et al. [11]. These authors compared a 22Cr duplex stainless steel (DSS) and a SDSS in pit-like-solutions as a function of the chloride content. The main difference between the two stainless steels was found at 7 N Cl^-, a concentration considered to be the threshold for salt film precipitation [11]. Higher Cl^- concentrations caused a metal salt film precipitation on the material, seen by a diffusion limiting current in the active region of the anodic polarization curves [16]. Arguably, salt film precipitation suggested conditions of stable localized corrosion propagation [17,18]. The estimated E_{crit} values differed by 20 mV with experimental $E_{R,Crev}$ measured with PD-GS-PD in neutral pH, demonstrating the ability of Galvele's model to estimate the critical potentials of commercially

available alloys. Others [7,10–12,14] have also successfully distinguished the effect of other alloy elements by conducting anodic polarizations in acidic chloride environments.

The objective of this work was to investigate the possible role of W in a propagating localized attack as a function of temperature in simulated crevice electrolytes. For this purpose, two commercial SDSS differing mainly in their W content were tested in two different crevice-like environments as a function of temperature. Galvele's critical acidification model was employed to estimate theoretical E_{crit} values, which were compared with $E_{R,Crev}$ results obtained in neutral chloride solutions.

2. Materials and Methods

2.1. Materials

Two SDSS, differing mainly in their W composition, were studied in this work, namely UNS S32750 (W-free) and UNS S39274 (2.1 wt.% W). Table 1 summarizes their composition given by the provider and confirmed by EDS. Both materials were produced as extruded pipes with 30 mm wall thickness and 203.2 mm in diameter. Round samples were machined by first extracting cylinders along the length of the pipe. The thickness of the coin-shaped specimens was 3 mm and the diameter 25 mm for UNS S32750 and 30 mm for UNS S39274.

Table 1. Chemical composition in wt.%.

Material (UNS)	PRE_N [1]/$PRE_{N,W}$ [2]	C [3]	Si	Mn	S [3]	Cu	Ni	Cr	Mo	N	W	Fe
S32750	43/43	0.03	0.27	0.5	0.02	0.14	6.42	25.6	3.83	0.3	-	62.9
S39274	40/43	0.02	0.24	0.7	0.02	0.52	6.3	24.9	3.1	0.29	2.1	61.8

[1]—PRE_N = % Cr + 3.3% Mo + 16% N; [2]—$PRE_{N,W}$ = % Cr + 3.3 (% Mo + 0.5% W) + 16% N; [3]—Composition reported according to the alloy provider.

UNS S39274 was received in the solution annealed condition (heat-treated at 1085 °C for 10 min). UNS S32750 was solution annealed after machining, in an air-furnace at 1100 °C for 15 min and quenched in water, following the recommendations from the supplier.

Specimens were wet-ground down to 600 US-grit SiC paper, rinsed in acetone, followed by distilled water and ethanol, and cleaned in an ultrasonic bath for 5 min while they were immersed in ethanol.

Specimens of the two SDSSs were etched following Statoil technical note MAT-2010080 [19] to reveal the microstructure and distinguish the austenite (γ) and ferrite (α) phases by light optical microscopy (LOM) and scanning electron microscopy (SEM). The etching procedure consisted of two different steps. In the first step, a 15 wt.%. KOH solution was used, and a potential of 3 V was applied for 12 s. In the second step, the solution was 20 wt.%. NaOH with an applied potential of 1.5 V for 10 s. Figure 1 shows the microstructure of each material after the heat treatments. The γ and α ratio in these materials was measured by electron backscatter diffraction (EBSD) in a previous work [5], obtaining a 57.2 and 47.6 vol.% α for UNS S32750 and UNS S39274, respectively. These values are within the acceptable 40 to 60 vol.% range for each phase in SDSS. The average austenite region size of each material was determined by measuring the area of each austenite region in a minimum of three different areas and calculating the mean value by an open-access image processing software. The average austenite region size results for UNS S32750 and UNS S39274 were 577.9 μm^2 and 395.0 μm^2, respectively.

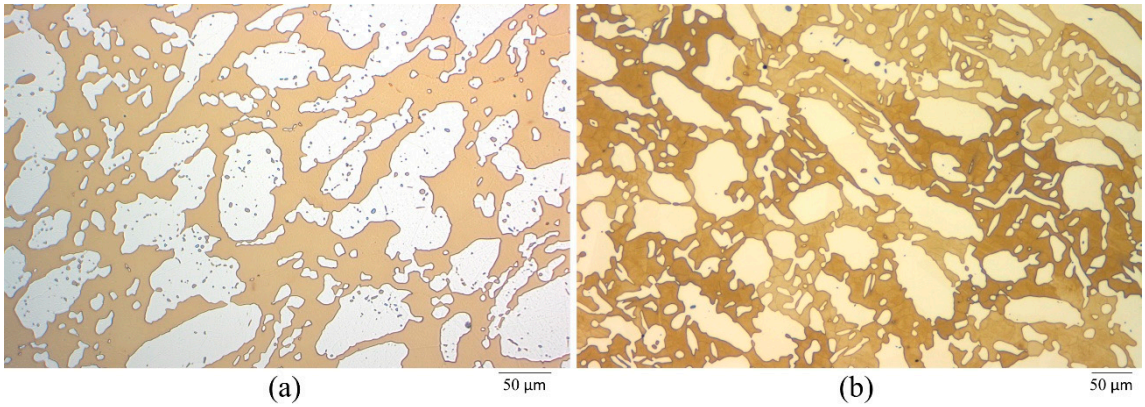

Figure 1. Light optical microscopy (LOM) micrographs of (**a**) UNS S32750, and (**b**) UNS S39274 after the heat treatments.

2.2. Galvele's Critical Acidification Model

Galvele's critical acidification model [13], described in Equation (1), can be used to estimate the E_{crit} when the concentration of aggressive specimens in the electrolyte is known. Henceforth, to simplify the model, E_{inh} is considered negligible to the contribution of E_{crit} [11]. Despite the release of potential inhibiting species such as molybdates and tungstates from the alloys during dissolution [20–22], it is considered acceptable as the E_{crit} value estimated in this manner is more conservative, i.e., lower E_{crit}. Thus, E_{crit} can be expressed as:

$$E_{crit} = E_{corr}{}^{*} + \eta + \phi \quad (2)$$

The ohmic potential drop term was estimated after Bocher et al. (Equation (3)) [11,14]:

$$\phi = \frac{\rho \cdot i_{crit} \cdot x^2}{2w} \quad (3)$$

where ρ is the resistivity in the solution and is assumed to be 10 Ω·cm [14], w is the crevice gap which was given a value of 1 µm [11], x is the diffusion distance considered to be 10^{-4} cm [23], and i_{crit} was obtained from the pit stability product (Equation (4)) [24]:

$$x \cdot i_{crit} = k \quad (4)$$

where k is a constant that is a function of the metal and pH of the solution. In this work and based on Kappes et al., the value of 10^{-6} A/cm was adopted [23]. Equations (3) and (4) yield an $i_{crit} = 10^{-2}$ A/cm^2 and $\phi = 5$ µV. Since the $\phi << E_{corr}{}^{*}$, E_{crit} can be obtained as:

$$E_{crit} = E_{corr}{}^{*} + \eta \quad (5)$$

$E_{corr}{}^{*}$ can be found by measuring the corrosion potential in an electrolyte simulating the inside of a corroding pit or crevice. Consequently, the E_{crit} can be obtained from Equation (5) by performing anodic potentiodynamic polarizations in crevice-like-solutions and obtaining the E_{corr} and η (i.e., the applied overpotential needed to reach $i_{crit} = 10^{-2}$ A/cm^2).

2.3. Crevice-Like-Solutions

Anodic potentiodynamic polarization experiments were conducted in solutions simulating pit/crevice environments. Two different crevice-like-solutions were used: 1 M HCl (as a reference solution at pH = 0) and 7 M LiCl, which was chosen based on Kappes et al. [11] as 7 N Cl^- presented the highest current density before salt precipitation occurred. The 7 M LiCl solution was adjusted to 0 pH by adding concentrated HCl, following the relationship between H^+ and Cl^- activity coefficients

given by Bocher et al. [14]. The volume used in each experiment was 160 mL, which was measured by a graduated cylinder. The solution resistances varied from the less conductive to the more conductive solutions from 0.3 to 0.1 Ω, which was also confirmed using OLI simulations (OLI SYSTEMS INC., Parsippany, NJ, USA) and in line with the work of Artemov et al. [25], who studied the conductivity of aqueous HCl, NaOH and NaCl solutions. Thus, the effect of IR drop was considered negligible for the comparative assessment of the two SDSSs.

A three electrode-cell consisting of an Ag/AgCl KCl saturated reference electrode (RE) (−199 mV vs. Standard Hydrogen Electrode–SHE-) immersed in the solution through a glass tube and kept at room temperature was used to carry out the anodic polarization tests. The counter electrode (CE) consisted of a Pt mesh. A commercially available electrochemical Avesta cell was used to avoid crevice corrosion [26], which was modified, as shown in Figure 2. In the original design of the Avesta cell, the distilled water required to avoid crevice corrosion flows into the main chamber, which might affect the pH and Cl^- concentration at the surface. The modification consisted of creating an additional outlet for the distilled water supplied by the peristaltic pump (Figure 2) to avoid contact with the electrolyte.

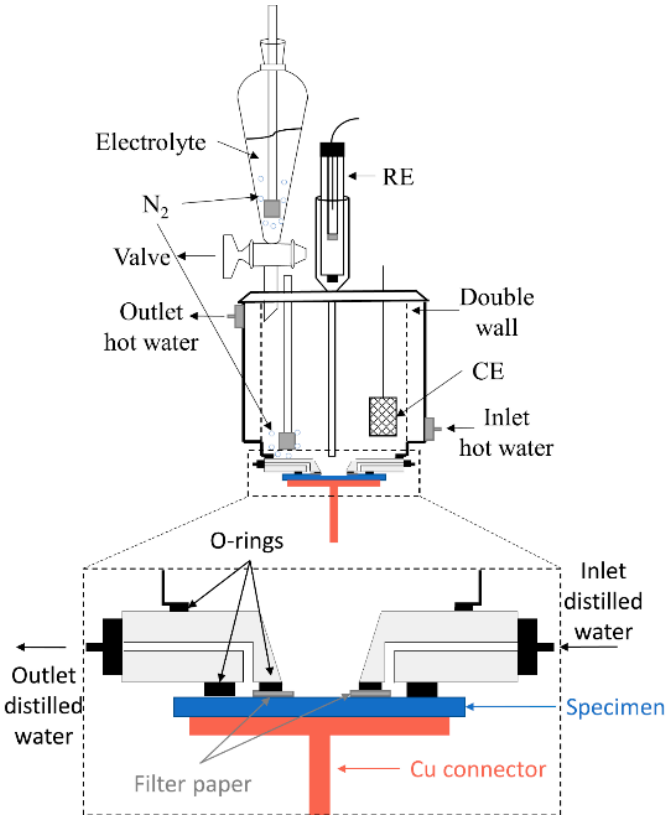

Figure 2. Full electrochemical test set-up showing the glass vessel employed to deaerate the electrolyte before introducing it into a pre-deaerated modified Avesta cell. The bottom part of the cell (the part with the inlet/outlet of the distilled water, the filter paper, the specimen and Cu connector) is zoomed in to show the particular features of the Avesta cell. The drawing is not to scale.

Consequently, the distilled water did not leak into the electrolyte, but circulated through the O-ring sealing, wetting the filter paper and, then, circulated outside the cell through a new vent. The area of the working electrode was 1.54 cm^2.

Anodic polarization experiments were performed at different temperatures: room temperature (22 ± 1 °C), 40 °C, 50 °C, and 60 °C. The temperature was controlled using a water bath connected to the double glass wall of the cell, except for the room temperature condition in which testing was done at the temperature of the lab.

The tests were performed in an oxygen-free electrolyte since the localized environment inside active pits and crevices has a low oxygen content, as it is consumed during the initial stages [27]. The electrolyte was purged with nitrogen gas for 1 h before exposing the specimen to ensure a low dissolved oxygen concentration. Since the specimen is placed at the bottom of the cell (Figure 2), the electrolyte had to be purged in a tight glass vessel mounted on top of the Avesta cell, as illustrated in Figure 2. The main Avesta cell chamber was simultaneously purged with N_2 to remove all air and ensure an O_2-free atmosphere from the moment the solution came in contact with the specimen. The tight glass vessel was connected through a valve directly into the Avesta cell, to avoid contact of the deaerated electrolyte with the air when transferring the solution from the vessel to the main cell. Deaeration of the electrolyte continued during the tests. The dissolved oxygen concentration was monitored continuously using a fiber optic oxygen meter, and its content was always below 10 ppb from the moment the material came in contact with the test solution.

The sequence of the anodic polarization tests was as follows. First, the $E_{corr}{}^{*}$ was measured for 1 h (the asterisk indicates that E_{corr} was measured in a simulated crevice solution), followed by the anodic potentiodynamic polarization, starting at $E_{corr}{}^{*}$ and finishing at 1.2 $V_{Ag/AgCl}$, with a sweep rate of 0.167 mV/s. All tests were performed at least in duplicate.

The passive current density (i_{pass}), the critical passive current density (i_{cp}), the corrosion potential ($E_{corr}{}^{*}$), the transpassive potential (E_{Trans}), and the primary passive potential (E_{pp}) were obtained from each anodic potentiodynamic polarization curve.

2.4. Characterization

After the tests, the electrolyte was stored in tight plastic containers and the ions released from the specimens were quantified using Inductively Coupled Plasma Mass Spectrometry (ICP-MS).

Congruent or incongruent dissolution was verified with the ICP-MS results by calculating the dissolution ratio of each metallic element M (d'_M). d'_M was defined as the ratio between the experimental dissolution ($d_{experimental}$) quantified by the ICP-MS analysis and the congruent dissolution ($d_{congruent}$) value. $d_{congruent}$ was calculated as the proportional dissolution of Fe, as it is the bulk element for the two materials, as shown in Equation (6):

$$d'_M = \frac{d_{M.experimental}}{d_{M.congruent}} = \frac{d_M}{\frac{C_M . d_{Fe}}{C_{Fe}}}, \quad (6)$$

where d_M (in ppb) is the dissolution quantity of metal M measured by ICP-MS, C_M (in wt.%) is the concentration in solid solution of metal M in the material (shown in Table 1), C_{Fe} (in wt.%) is the concentration in solid solution of Fe in the material (shown in Table 1), and d_{Fe} (in ppb) is the dissolution quantity of Fe obtained by ICP-MS for the same condition as that of the measured metal M. In this regard, a $d'_M > 1$ suggests selective metal M dissolution [28]. Contrarily, a $d'_M < 1$ implies a relative surface enrichment in M [28]. Finally, $d'_M = 1$ indicates congruent dissolution [28].

The specimens were analyzed after the tests with an infinite focus microscope (IFM) used as a LOM, which can simultaneously acquire the 3D surface profile, enabling the estimation of the depth of localized attacks. The specimens were also analyzed by SEM together with energy-dispersive x-ray spectroscopy (EDS). An accelerated voltage of 20 kV, with a 50 µm diameter aperture and a spot size of 5 was employed, giving a beam current of approximately 7.2 nA. The point analysis tool was used to acquire the composition of the full area taken by the SEM. At least five measurements were performed per specimen.

2.5. Statistical Analysis

A statistical study of the data was performed to examine whether the metal cations quantity released at the end of the electrochemical test was related to any of the polarization curve parameters or the two parameters, η and E_{crit}, used in Galvele's model. The statistical study consisted of calculating the Kendall

correlation coefficient [29] in a pairwise comparison between all the mentioned variables. In contrast to other more known correlation parameters such as Pearson's, the Kendall correlation coefficient does not assume a normal distribution [30]. Thus, Kendall's coefficient indicates a general monotonic relationship, i.e., if both variables increase or decrease together [29]. Consequently, Kendall's coefficient will show a strong relationship even for non-linear relationships such as exponential behaviors.

For this reason, this coefficient is becoming more popular within the scientific community [29,31]. The closer the coefficient is to 1 (in absolute value), the stronger the variables are connected. The sign of the coefficient indicates the type of relationship: (i) positive; both variables increase or decrease together, or (ii) negative, one variable increases as the other decreases.

3. Results

3.1. Crevice-Like-Solutions

Figure 3 illustrates how i_{pass}, i_{cp}, E_{pp}, $E_{corr}{}^{*}$, and E_{Trans} values were obtained from the anodic potentiodynamic polarization curves. Figure 4 summarizes the anodic potentiodynamic polarization curves obtained for one specimen of each alloy tested at each temperature, while Figure 5 presents all the critical parameters extracted from Figure 4. As indicated in Figure 3, i_{pass} was calculated as the average value between the intersections between lines 1 and 2 at low potentials and the intersection of lines 3 and 4 at high potentials. Although the limiting currents after the active/passive transition do not imply true passivation given the high values, i_{pass} was calculated as the average value of the current density measured during the pseudopassive region following the same criteria as for the normal passive range. In agreement with others [11,32], i_{cp} was obtained as the maximum current density measured before the active/passive transition. Similarly, E_{pp} was defined as the potential at which the transition from active to passive took place. $E_{corr}{}^{*}$ was considered as the value measured at the end of the 1 h open circuit potential measurement before polarization. After the active/passive transition, potentials reached values more positive than the oxygen evolution reaction and within the transpassive area [33]. Consequently, the inflection point seen at high anodic potentials (the intersection between lines 3 and 4 in Figure 3) was defined as E_{Trans}.

As shown in Figures 4 and 5, a clear difference was observed between the two solutions. In this regard, the active/passive transition in 1 N Cl^{-} was only observed at T ≥ 40 °C and T = 60 °C for UNS S32750 and UNS S39274, respectively. In contrast, active dissolution followed by a high diffusion-limited current ($i_{lim} \approx i_{cp}$) and passivation at E_{pp} occurred in 7 M LiCl for all specimens at all temperatures. Even though the current density did not achieve typical passive values, this area will be referred to as passive hereunder to compare i_{pass} between the solutions. Additionally, lower current densities (both i_{cp} and i_{pass}) were obtained in 1 M HCl for potentials below the oxygen evolution reaction or below the transpassive region [33]. In contrast, i_{pass} was, in most cases, as high in 1 M HCl as in 7 M LiCl for UNS S32750. In 7 M LiCl, the E_{pp} values were nobler than in 1 M HCl. In fact, due to the high $E_{corr}{}^{*}$ values in 1 M HCl, the E_{pp} was not observed in several tests, as indicated in Figure 5.

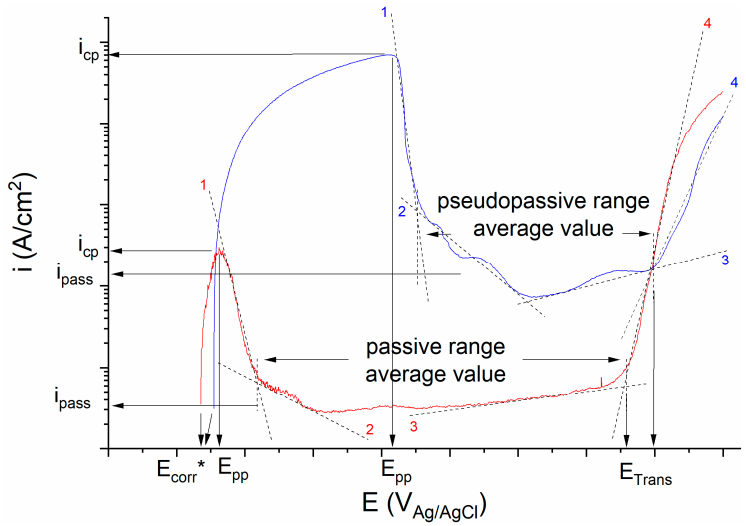

Figure 3. Illustration of the parameters obtained from anodic polarization curves for the tests performed in 1 M HCl and 7 M LiCl at pH 0.

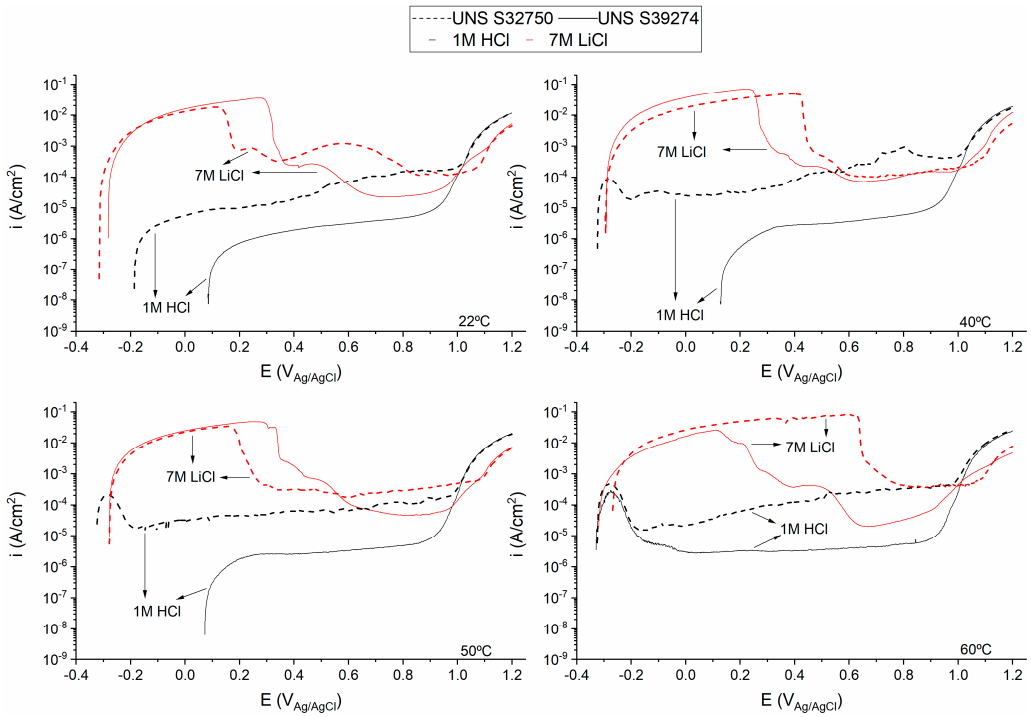

Figure 4. Anodic potentiodynamic polarization curves in two crevice-like-solutions as a function of temperature, as indicated.

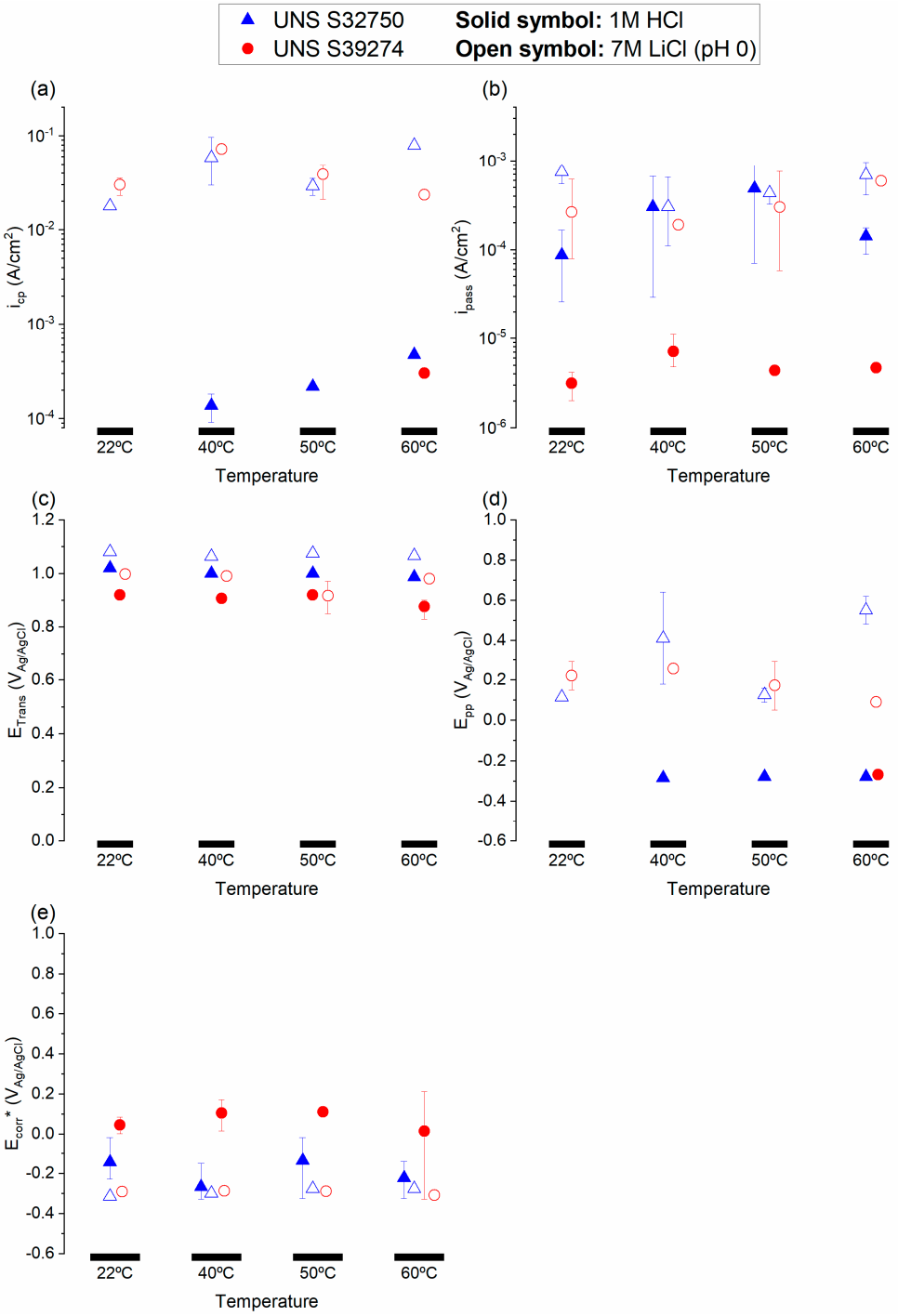

Figure 5. (**a**) i_{cp}, (**b**) i_{pass}, (**c**) E_{Trans}, (**d**) E_{pp}, and (**e**) E_{corr}* measured from the anodic potentiodynamic polarization tests. Error bars indicate maximum and minimum values.

Differences between the two materials were also observed. In 1 M HCl, UNS S32750 had a higher i_{pass} than UNS S39274, whereas the E_{pp} of UNS S32750 was more positive in 7 M LiCl, especially at 60 °C. At that same temperature, there was a significant difference in i_{cp} between both materials in 7 M LiCl.

Figure 6 illustrates the surface of two specimens after exposure, as observed by LOM. No crevice corrosion was found along the edges of the filter paper by both high IFM magnifications and SEM analysis. No evident corrosion attack was seen on the surface of the specimens tested in 1 M HCl. In

this case, the surface was slightly etched, revealing the grain structure of the samples. In contrast and as expected [11], the specimens tested in 7 M LiCl experienced uniform dissolution.

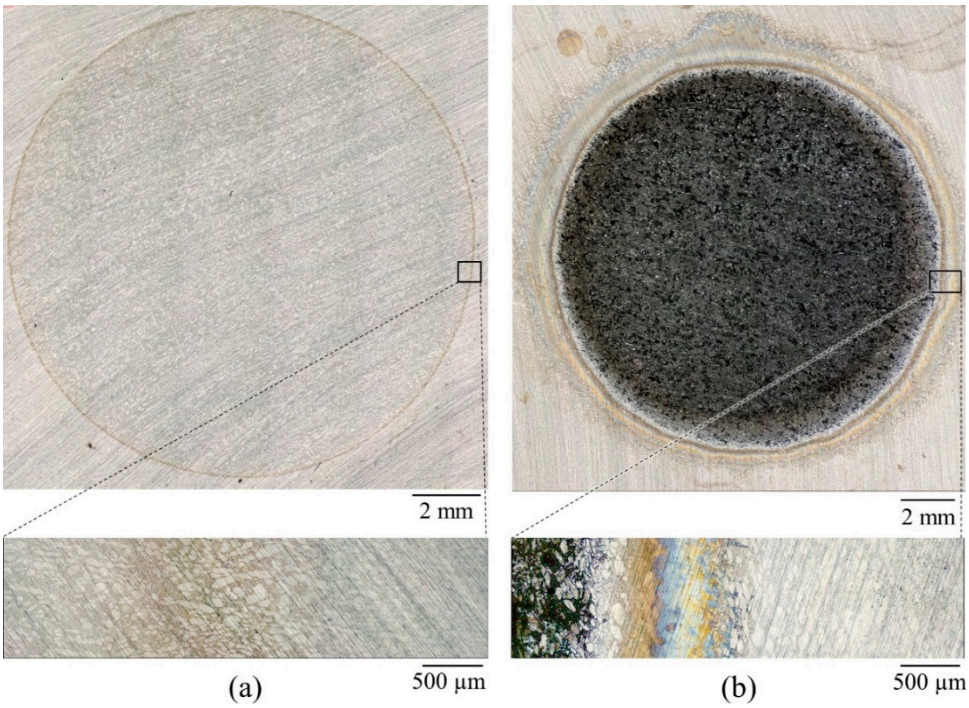

Figure 6. Optical visualization of UNS S39274 specimens after anodic potentiodynamic polarization at room temperature exposed to (**a**) 1 M HCl, and (**b**) 7 M LiCl. The exposed area, the circle, is equal in the two pictures.

The surface analysis performed by SEM and EDS of the corroded specimens in 7 M LiCl revealed a clear difference in the attack morphology between both SDSS. Figure 7 shows the morphology of the attack after testing, as observed by SEM. While both phases corroded uniformly in the case of UNS S32750, S39274 suffered selective dissolution of the α-phase. In this regard, ferrite can be distinguished easily from austenite using EDS due to its lower Ni and higher Cr and Mo concentration [6,34]. The surface chemical composition of each phase for both materials obtained by EDS before and after the corrosion testing is presented in Table 2. The W-free material showed a relative enrichment in O, Ni, and Mo and an impoverishment in Cr and, especially Fe, when comparing the values before and after the corrosion testing. This behavior was observed for both austenite and ferrite phases. On the other hand, the W-rich material was richer in O and Mo, but poorer only in Fe. In comparison, Cr and Ni concentration was similar before and after corrosion. Nevertheless, there was a difference in the W content between the austenite and ferrite phases. W was enriched in the ferrite phase, but not in austenite after corrosion.

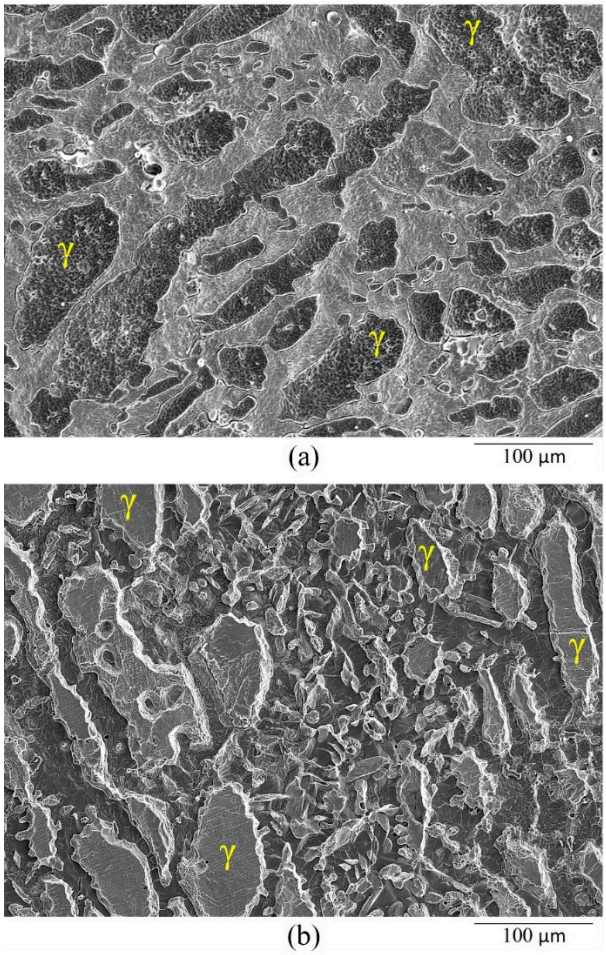

Figure 7. SEM secondary electron images of (**a**) UNS S32750, and (**b**) UNS S39274 specimens after the anodic potentiodynamic polarization in a 7 M LiCl solution at 60 °C. In the pictures, the austenite phase (γ) is indicated. The other phase is ferrite (α).

Table 2. Average surface chemical composition of the specimen in wt.% obtained by EDS before and after the anodic potentiodynamic polarization in 7 M LiCl at 60 °C.

-	Before Corrosion Testing				After Corrosion Testing			
Elements	**UNS S32750**		**UNS S39274**		**UNS S32750**		**UNS S39274**	
-	α	γ	α	γ	α	γ	α	γ
O	-	-	-	-	2.4	3.7	1.7	0.9
Cr	28.1	25.2	26.4	24.1	26.2	23.1	26.5	24.6
Fe	63.9	64.9	63.5	64.7	57.6	56.3	58.6	60.9
Ni	4.6	7.5	4.7	7.3	5.3	8.0	4.4	7.0
Mo	3.6	2.3	2.9	1.9	5.8	4.0	3.6	2.4
W	-	-	2.5	1.9	-	-	3.2	1.8

Figure 8 shows the concentration of dissolved metal cations as measured by ICP-MS after testing. As expected, the concentration of dissolved metal cations was larger in 7 M LiCl than in 1 M HCl for both materials, which increased with increasing temperature (except for UNS S39274 at 60 °C in 7 M LiCl). The amount of released metal cations by both materials in 1 M HCl was similar. Contrarily, in 7 M LiCl, the dissolved concentration of metal cations released by UNS S39274 was larger than that of UNS S32750, apart from the tests performed at 60 °C, where UNS S39274 experienced a much lower dissolution than UNS S32750.

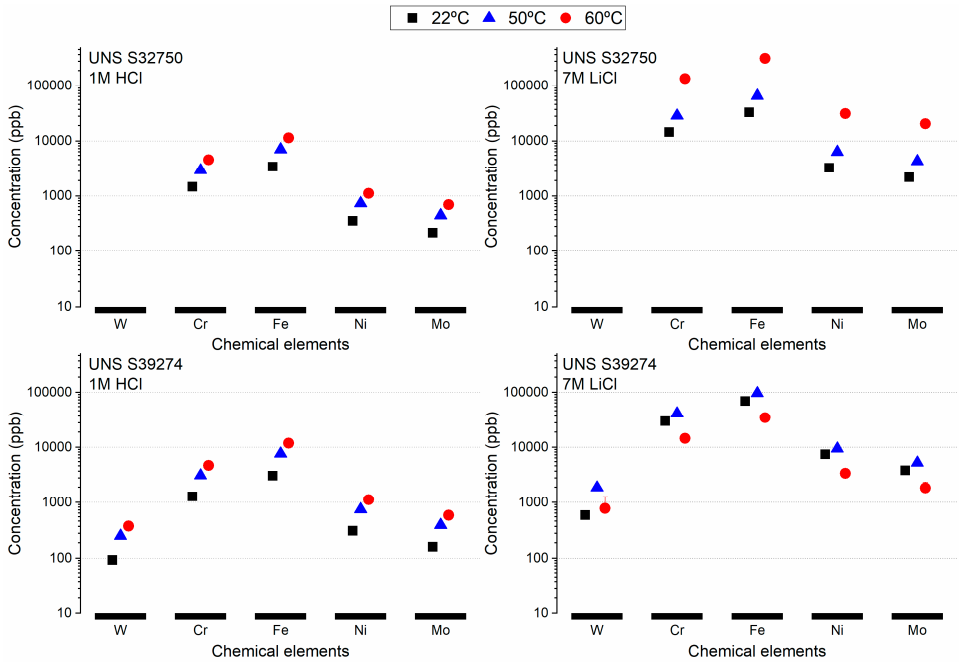

Figure 8. Concentration of dissolved metal cations measured by ICP-MS after performing the anodic potentiodynamic polarization tests. Error bars indicate maximum and minimum values. Due to the logarithmic scale, most of them are not visible.

Table 3 shows the calculated dissolution ratio (d'_M) of each element for all specimens. Cr, Ni, and Mo showed dissolutions ratios close to 1, suggesting congruent dissolution with Fe. On the other hand, there were significant differences regarding the dissolution ratio of W. In 1 M HCl, d'_W was close to 1; however, in 7 M LiCl, the results indicated a possible surface enrichment of W on the surface, as $d'_W < 1$.

Table 3. Normalized dissolution quantities (d'_M) for each element calculated from Equation (6), using the average concentration quantified by ICP-MS.

Material	Solution	T (°C)	d'_W	d'_{Cr}	d'_{Fe}	d'_{Ni}	d'_{Mo}
UNS S32750	1 M HCl	22	-	1.05	1.00	1.01	1.03
		40	-	1.01	1.00	0.98	1.03
		50	-	1.03	1.00	1.02	1.04
		60	-	0.99	1.00	0.96	1.00
	7 M LiCl	22	-	1.08	1.00	0.97	1.09
		40	-	1.02	1.00	0.97	1.06
		50	-	1.07	1.00	0.95	1.08
		60	-	1.05	1.00	0.96	1.06
UNS S39274	1 M HCl	22	0.90	1.04	1.00	0.99	1.05
		40	1.01	1.03	1.00	1.01	1.02
		50	0.96	1.01	1.00	0.96	1.02
		60	0.93	0.98	1.00	0.93	0.98
	7 M LiCl	22	0.25	1.07	1.00	1.06	1.10
		40	-	-	-	-	-
		50	0.57	1.06	1.00	0.96	1.08
		60	0.66	1.04	1.00	0.96	1.06

3.2. *Galvele's Acidification Model*

Figure 9 illustrates the $E_{corr}{}^*$ and η obtained from the anodic potentiodynamic polarization curves used for Galvele's critical acidification model, together with the estimated E_{crit} calculated using

Equation (5). Even though both materials differed in the $E_{corr}{}^{*}$ and η, the resulting E_{crit} was similar for both materials in 1 M HCl. Additionally, the estimated E_{crit} values were over the reversible potential of the oxygen evolution reaction and within the transpassive region [33], suggesting transpassive dissolution. As a result, in neutral chloride solutions, it could be expected that $E_{crit} \approx E_{Trans}$ at all temperatures. In 7 N Cl^{-}, there were no differences in most cases, apart from 60 °C where UNS S39274 obtained a slightly nobler E_{crit} than UNS S32750, due to the difference in η between materials. In all other conditions, E_{crit} decreased slightly with temperature, although the differences were within the experimental error.

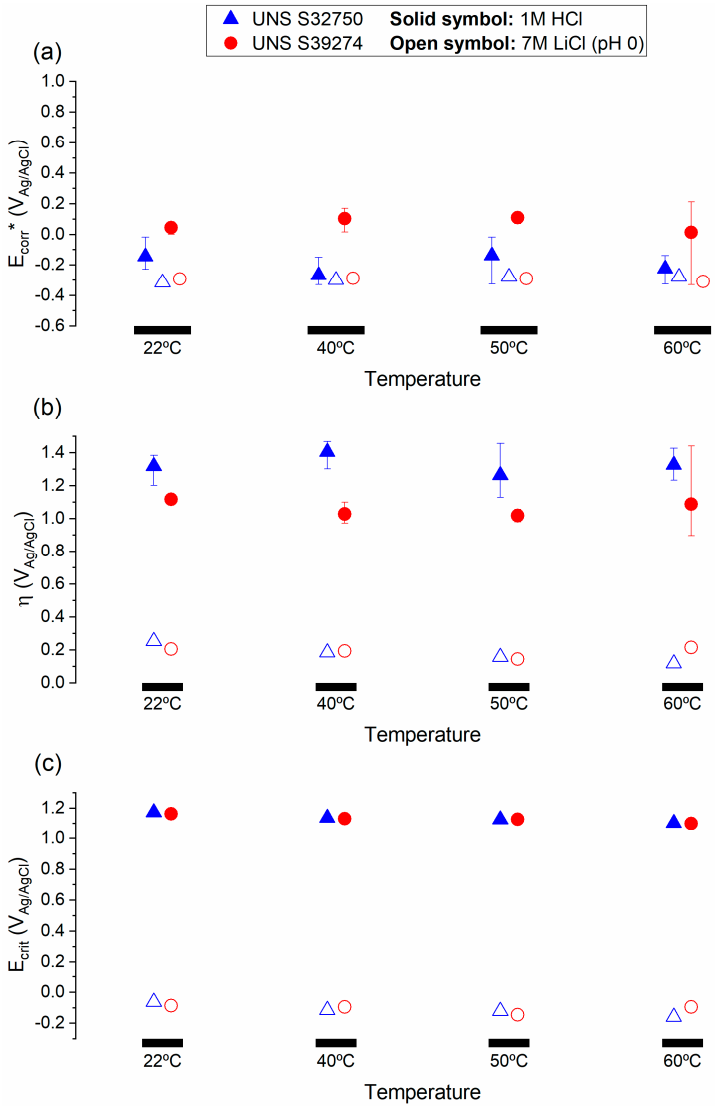

Figure 9. (**a**) $E_{corr}{}^{*}$ and (**b**) η obtained from the anodic potentiodynamic polarization curves in crevice-like-solutions to estimate (**c**) E_{crit} obtained by Galvele's critical acidification model. Error bars indicate maximum and minimum values.

3.3. Statistical Analysis

Tables 4 and 5 contain Kendall's correlation coefficients calculated for the pairwise parameters shown in the column and row of each cell for 1 M HCl and 7 M LiCl crevice-like-solutions, respectively. Additionally, statistically significant (p-value < 0.05) values are indicated in bold font.

In both electrolytes, the concentration of released metal cations of each element seemed to follow the same trend, either increasing or decreasing in quantity altogether. The only exception was W

in 7 M LiCl, which did not present any relationship with any parameter. The other elements had a strong significant positive relationship with i_{cp} and E_{pp} in 7 M LiCl. In contrast, in 1 M HCl, only a strong positive correlation was seen between the dissolution of the chemical elements and i_{cp}. The low correlation values obtained for E_{pp} were most likely due to the low number of tests where the E_{pp} could be measured, as it was mentioned above. E_{crit} was correlated to the concentration of dissolved elements, especially in 1 M HCl, indicating an increment of released cations of all elements, the more negative the E_{crit}. However, even though the correlation was weaker in 7 M LiCl, there was a significant exception since W was the only element with no relationship to E_{crit}.

Table 4. Kendall's correlation coefficient obtained for all tests performed in 1 M HCl. Bold numbers indicate a statistically significant (p-value < 0.05) correlation coefficient. (T stands for temperature).

-	Cr	Fe	Ni	Mo	T	i_{cp}	E_{Trans}	i_{pass}	E_{pp}	$E_{corr}{}^{*}$	E_{crit}	η
W	0.93	0.93	0.93	1	0.91	-	−0.65	0.00	-	0.07	−0.71	−0.21
Cr		1	0.99	0.91	0.80	1	−0.32	0.02	0.18	−0.09	−0.84	−0.02
Fe			0.99	0.91	0.80	1	−0.32	0.02	0.18	−0.09	−0.84	−0.02
Ni				0.93	0.78	1	−0.31	0.03	0.18	−0.10	−0.82	0.00
Mo					0.78	1	−0.24	0.10	0.18	−0.15	−0.75	0.04
T						0.82	−0.40	−0.05	0.67	0.00	−0.73	−0.10
i_{cp}							−0.55	−0.33	0.18	−0.33	−1	−1
E_{Trans}								0.56	−0.80	−0.42	0.35	0.50
i_{pass}									−0.91	−0.34	−0.09	0.35
E_{pp}										−0.18	−0.18	−0.18
$E_{corr}{}^{*}$											0.04	−0.90
E_{crit}												0.06

Table 5. Kendall's correlation coefficient obtained for all tests performed in 7 M LiCl. Bold numbers indicate a statistically significant (p-value < 0.05) correlation coefficient. (T stands for temperature).

-	Cr	Fe	Ni	Mo	T	i_{cp}	E_{Trans}	i_{pass}	E_{pp}	$E_{corr}{}^{*}$	E_{crit}	η
W	0.52	0.52	0.52	0.52	0.11	0.52	−0.59	−0.62	0.20	0.14	−0.33	−0.33
Cr		1	0.98	0.93	0.16	0.91	0.06	−0.32	0.75	0.30	−0.58	−0.63
Fe			0.98	0.93	0.16	0.91	0.06	−0.32	0.75	0.30	−0.58	−0.63
Ni				0.91	0.14	0.93	0.03	−0.34	0.77	0.28	−0.56	−0.60
Mo					0.11	0.85	0.12	−0.30	0.77	0.32	−0.52	−0.56
T						0.22	−0.17	0.14	−0.03	0.29	−0.34	−0.47
i_{cp}							−0.03	−0.32	0.75	0.30	−0.58	−0.63
E_{Trans}								0.43	0.12	0.03	−0.03	−0.03
i_{pass}									−0.24	−0.10	0.08	0.12
E_{pp}										0.18	−0.33	−0.38
$E_{corr}{}^{*}$											−0.36	−0.54
E_{crit}												0.82

4. Discussion

4.1. Choice of Parameters for the Critical Acidification Model

During stable pit and crevice propagation, Cl^- anions migrate inside the pit/crevice to maintain electroneutrality as the metal cations are released at the bottom of the attack and undergo hydrolysis [27,35]. Therefore, different Cl^- concentrations simulate different propagation degrees. The Cl^- concentration is limited by the metallic cation saturation concentration, above which a metallic salt film precipitates [11]. Some authors have reported maximum Cl^- concentration values in artificial and real pits of 6 N [9] and 12 N Cl^- [36], respectively. Additionally, Kappes et al. [11] reported the precipitation of the salt film in a 22Cr DSS and UNS S32750 to occur between 7 N and 9 N Cl^-, representing the 58% and 75% Cl^- saturation concentration, respectively. Other authors [15,37] calculated the critical saturation concentration to be 50% for UNS S31600, i.e., approximately 7 N Cl^-

concentration required for stability of localized corrosion. Kappes and coauthors [11] observed as well that the maximum current density (i_{cp}) decreased with higher Cl^- content above the saturation concentration. On the other hand, i_{cp} increased with Cl^- concentration in the range below salt film formation. In this regard, the 7 N Cl^- concentration solution was chosen in this work to study the effect of W for being the crevice-like-solution with the highest i_{cp}. Similarly, the pH inside artificial pits has been reported to be close to 0 [9], becoming the pH value employed by Kappes et al. [11] and the chosen pH value in this work.

Galvele [13] developed the critical acidification model for pure metals; hence, the choice of parameters, especially for the stability product, must differ when estimating E_{crit} in alloys. Bocher et al. [14] employed a stability product value of $x \cdot i_{crit}$ = 0.01 A/cm, with x = 0.001 cm for Ni-alloys. This choice of parameters results in i_{crit} = 10 A/cm^2, a current density value four orders of magnitude larger than the i_{crit} determined by Kappes [11] and in this work. Additionally, 10 A/cm^2 in the anodic potentiodynamic curves can only be reached in transpassive potentials, as seen in Figures 4 and 5, erroneously implying that both SDSS would be immune to crevice corrosion at all temperatures. In this regard, the i_{crit} obtained in this work, similar to the one calculated by Kappes [11], were considered to be more appropriate for the estimation of E_{crit} in DSS.

4.2. Role of W in Crevice-Like-Solutions

The theoretical E_{crit} values obtained from Galvele's critical acidification model demonstrate the large difference in the aggressiveness of the solutions, as expected. The E_{crit} values obtained in 1 M HCl where all more positive than the oxygen evolution reaction [33], implying that stable localized corrosion requires a higher chloride concentration and, thus, the material will suffer transpassive dissolution, i.e., E_{crit} in 1 N Cl^- is, in reality, an E_{Trans}. In contrast, E_{crit} values for 7 N Cl^- were low, suggesting that crevice corrosion could be possible in neutral chloride environments at all the temperatures investigated. Interestingly, Figure 8 clearly shows a significant difference in the concentration of dissolved ions in the two solutions, with much higher values for all elements in 7 M LiCl.

Both materials behaved similarly in the 1 N Cl^- environment. All parameters from the anodic potentiodynamic polarizations were in the same range (Figures 4 and 5), with the only exception of $E_{corr}{}^*$ and i_{pass}, which were lower and higher, respectively, for UNS S32750, indicating a lower corrosion resistance in the pit/crevice solution. However, the concentration of dissolved metal cations was similar in both SDSSs (Figure 8). Since the anodic potentiodynamic polarization in all tests reached the transpassive region, it is suspected that most of the ions were released at these high potentials, causing negligible dissolution in the passive region or at $E_{corr}{}^*$.

In the more aggressive 7 M LiCl solution, both materials showed larger differences, especially at 60 °C. Even though all parameters extracted from the anodic potentiodynamic polarization curves (Figure 4) were in the same range up to 50 °C, the concentration of released ions was higher in UNS S39274 than in UNS S32750. Nevertheless, at 60 °C, UNS S39274 showed a somewhat better corrosion resistance as indicated by i_{cp}, $E_{pp,}$ and the lower concentration of dissolved cations.

Based on the concentration of dissolved metal cations, the d'_M reported in Table 3 indicates an important difference that can be related to the difference achieved in E_{crit} for the two solutions. The only values that changed significantly between the solutions were d'_W at all temperatures. In 1 M HCl, d'_W was between 0.9 and 1, suggesting congruent W dissolution, similar to the other elements. In contrast, in 7 M LiCl, d'_W fluctuated between 0.25 and 0.66, depending on the temperature, suggesting a surface enrichment in W. Indeed, W was the only element displaying incongruent dissolution, as all the other elements dissolved approximately uniformly at all temperatures. According to the Pourbaix diagrams [33], W is the only element capable of forming an oxide layer, WO_3, at pH 0. Indeed, a yellow (the color of WO_3 [33]) reflection was seen on UNS S39274 after the tests. Even though W is a ferrite stabilizer [38], ferrite dissolved selectively for UNS S39274, as seen in Figure 7. The dissolved W, in the form of tungstate ions, can precipitate forming a WO_3 layer, shown to reduce the corrosion rate [39]. A small enrichment was measured by EDS (Table 2) in ferrite, but not on austenite. Most likely, given

the small thickness of the deposit, a more surface-sensitive technique such as x-ray photoelectron spectroscopy (XPS) or Auger electron spectroscopy (AES) would be needed to confirm this assumption. On the other hand, the W-free material showed a uniform attack, as illustrated in Figure 7.

The analysis of the chemical composition of the phases before corrosion included in Table 2 showed that both α and γ phases of UNS S32750 are richer in Cr (>1 wt.%) and Mo (approximately 0.5 wt.%) than the phases in UNS S39274. The total wt.% (Cr + Mo) difference between the two SDSSs for each phase was approximately the same as the content of W in UNS S39274 of that phase. Nevertheless, variances in chemical composition alone cannot explain the difference in the corrosion morphology observed by SEM (Figure 7). Local probe technique studies of passive film have concluded that, despite the higher PRE value of the ferrite phase in SDSS, austenite shows a more noble behavior, i.e., austenite is more corrosion resistant than ferrite [40]. However, when the material was exposed to a very aggressive environment (i.e., concentrated nitric acid), both austenite and ferrite adopted similar passive film properties and their differences disappeared. This observation is in line with the uniform corrosion observed in 7 M LiCl solution at 60 °C of UNS S32750 in this work. Nevertheless, the selective dissolution of ferrite observed for UNS S39274 is not in line with the SKPFM results obtained by Rahimi et al. [41], where ferrite showed a nobler behavior than austenite. On the other hand, selective dissolution of ferrite of SDSS was observed by Långberg et al. [42] as the data obtained by synchrotron XRR, XRF, and XRD showed a higher dissolution quantity of Fe from ferrite than austenite. Additionally, this work observed the following order in element dissolution in UNS S32750 as the potentiodynamic polarization applied higher potentials: only Fe at $E < 1$ $V_{Ag/AgCl}$, then dissolution of Fe and Cr at $E > 1.2$ $V_{Ag/AgCl}$ causing an enrichment of Mo and Ni and, finally, dissolution of all elements at $E > 1.3$ $V_{Ag/AgCl}$. This dissolution order fits the behavior seen for UNS S32750 in Table 2, where the surface was enriched in Ni and Mo and depleted in Cr and, especially, Fe. However, Rahimi et al. [41] stated that W promotes the stability of Mo, Cr and Fe. This statement can explain why the W-rich material experimented no Cr impoverishment and a much lower dissolution of Fe than the W-free material.

The improved localized corrosion resistance of UNS S39274 at 60 °C, indicated by the lower metallic cation dissolution (Figure 8), the lower i_{cp}, and higher E_{pp} (Figures 4 and 5), resulted in a higher E_{crit} calculated by Galvele's critical acidification model (Figure 9). The E_{crit} value obtained was nobler (approximately 100 mV) than that of UNS S32750, and nobler than the E_{crit} at previous temperatures. The increase of E_{crit} at 60 °C was mainly due to the shift of η to more noble potentials. As stated by Galvele et al. [7], an increment of η indicates a slower dissolution rate.

Kendall's correlation coefficient calculated in Tables 4 and 5 also showed a significant difference between the quantity of W dissolved into the electrolyte and E_{crit} in 7 M LiCl. The correlation between the dissolution of Cr, Fe, Ni, and Mo and E_{crit} is seen in Figures 8 and 9. Up to 50 °C, the dissolution of these elements increased, whereas the E_{crit} decreased. However, at 60 °C, this behavior changed for both parameters. The dissolution of the elements was reduced, whereas E_{crit} increased. In other words, at all temperatures, the dissolution quantity and the E_{crit} followed exactly the opposite trend, reflected by a strong negative value of Kendall's coefficient.

The fact that W was not correlated in the same way as the other elements might suggest that; either (i) W dissolution increased even though E_{crit} was nobler for UNS S39274 than for UNS S32750, or (ii) W dissolution decreased as E_{crit} decreases for UNS S39274. Even though Figure 8 shows that W dissolution decreased at 60 °C in 7 M LiCl, as the other elements, whereas d'_W (Table 3) indicated that W was released in higher amounts at that condition. The only plausible explanation is that the dissolution of W was reduced, but not as much as the other elements at 60 °C in 7 M LiCl. This increment in d'_W despite the nobler E_{crit} at this particular condition for UNS S39274 is most likely the reason why the dissolution of W and E_{crit} were not correlated. Consequently, the combination of d'_W and Kendall's coefficient parameters infer a significant role of W on the improvement of corrosion resistance in propagating localized attacks, i.e., 7 N Cl^- acidic environments, only at 60 °C.

4.3. Prediction of Crevice Corrosion Repassivation Potential

In this work, Galvele's model was used to estimate the theoretical E_{crit} in different crevice-like-solutions and to study the validity of the model to predict crevice corrosion potentials, more specifically $E_{R,Crev}$ as it is widely used to define a protection potential [6]. Figure 10 compares E_{crit} values estimated by the critical acidification model in this work and by Kappes et al. [11] with experimental $E_{R,Crev}$ results of UNS S32750 and UNS S39274 measured by the PD-GS-PD technique in 3.5% NaCl (pH = 6.5) by Torres et al. [6]. In this regard, Torres et al. established a $T_{R,Crev}$ = 55 °C for UNS S39274 in 3.5 wt.% NaCl by the PD-GS-PD technique. In the same study, UNS S39274 polarized at +600 $mV_{Ag/AgCl}$ (simulating chlorinated seawater [43,44]) gave a CCT of 55 °C in natural seawater. For UNS S32750, that same work measured a CCT of 45 °C and a $T_{R,Crev}$ of 42.5 °C in natural seawater polarized at +600 $mV_{Ag/AgCl}$.

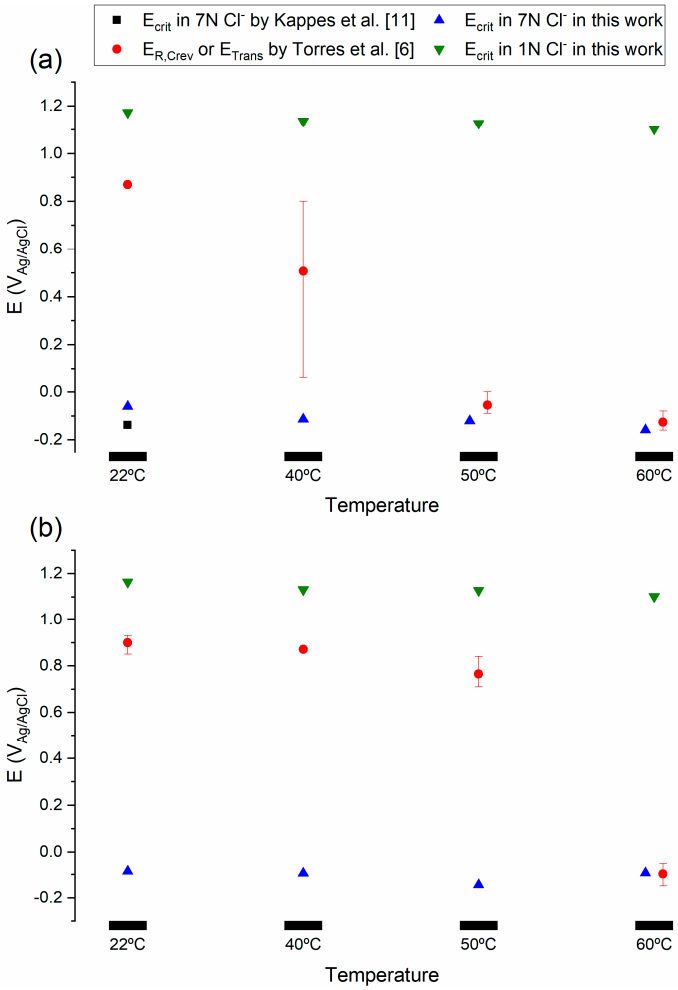

Figure 10. A comparison of estimated E_{crit} and measured $E_{R,Crev}$ for (**a**) UNS S32750, and (**b**) UNS S39274, as shown. Error bars indicate maximum and minimum values.

As seen in Figure 10, the E_{crit} estimate by Kappes et al. [11] for UNS S32750 at room temperature in 7 M LiCl was approximately 70 mV less noble than the one obtained in this work. Additionally, the difference between the E_{crit} value reported by Kappes and the $E_{R,Crev}$ of UNS S32750 in 1 wt.% NaCl environment at 30 °C reported by Martinez et al. [45] is only of 20 mV, whereas the difference increases to 90 mV when compared to the E_{crit} obtained in this work. Nevertheless, many studies have tested SDSS, in particular UNS S32750, obtaining critical temperatures (T_{crit}) for localized corrosion well

above 30 °C [43,46–49], i.e., E_{crit} is within the transpassive region at T ≤ 30 °C, differing significantly from the E_{crit} values measured by Kappes and Martinez et al.

In this work, the E_{crit} values obtained using Galvele's model were independent of temperature and suggested the possibility of crevice corrosion at T ≥ 22 °C. In contrast, PD-GS-PD results gave E_{crit} values in the transpassive range for T < $T_{R,Crev}$, which was 40 °C for UNS S32750 and 55 °C for S39274. The discrepancy can be reconciled by the fact that Galvele's model describes stable localized corrosion propagation. The high potentials measured by the PD-GS-PD method in 3.5 wt.% NaCl suggested that crevice corrosion initiation is controlled by the breakdown of the passive film at T ≤ $T_{R,Crev}$ (or CCT) as suggested by the Li-Scully-Frankel framework [50,51]. In this regard, while crevice corrosion could propagate stably if the concentration of the crevice environment reaches 7 N Cl^-, in practice, the stability of the passive film at T < T_{crit} is rate-determining, preventing the development of the critical environment required for crevice corrosion propagation. To our knowledge, the effect of temperature on the critical acidification model has not been addressed to date. Despite these discrepancies, the E_{crit} obtained by Galvele's critical acidification model was in excellent agreement with $E_{R,Crev}$ values measured by the PD-GS-PD method in 3.5 wt.% NaCl (pH = 6.5) as seen in Figure 10, i.e., 33 mV difference at 60 °C and a 66 mV difference at 50 °C for UNS S32750, and no difference for UNS S39274 at 60 °C. These findings, therefore, also suggest that the use of the critical acidification model to estimate the theoretical E_{crit} might require prior knowledge of T_{crit}.

5. Conclusions

In this work, simulated crevice environments were tested, and Galvele's critical acidification model applied to estimate E_{crit} values as a function of temperature and study the effect of W as an alloying element in solid solution. The following conclusions were drawn:

- A 7 N Cl^- (pH = 0) crevice-like solution was necessary to simulate stable crevice propagation, suggesting that W additions could be beneficial only in situations of localized corrosion propagation under a salt film.
- The dissolution morphology was different between materials in 7 N Cl^-. UNS S32750 experienced uniform corrosion of austenite and ferrite phases, whereas α-phase selectively dissolved in UNS S39274.
- E_{crit} values obtained using the critical acidification model were independent of temperature, which contrasted with previous findings in simulated seawater environments. In line with the new Li-Scully-Frankel framework, the discrepancy was attributed to the stability of the passive film as a rate-determining step below a T_{crit}. Conversely, E_{crit} values obtained by the critical acidification model were in good agreement with $E_{R,Crev}$ results obtained by the PD-GS-PD technique in 3.5 wt.% NaCl for temperatures above $T_{R,Crev}$.

Author Contributions: Conceptualization, C.T., M.I. and R.J.; methodology, C.T., M.I., and R.J.; validation, C.T.; formal analysis, C.T.; investigation, C.T.; resources, C.T.; data curation, C.T.; writing—original draft preparation, C.T.; writing—review and editing, M.I. and R.J.; visualization, C.T.; supervision, M.I., and R.J.; project administration, R.J.; funding acquisition, R.J. All authors have read and agreed to the published version of the manuscript.

Funding: This research received no external funding.

Acknowledgments: The authors thank the help of Mariano Kappes (Comisión Nacional de Energía Atómica, CNEA, Argentina) for his guidance at the beginning of the project, especially with the crevice-like-solutions; Szymon Bernat (Sintef) for his help in the mechanical workshop with the modifications performed to the Avesta cell and Syverin Lierhagen (NTNU) for performing the ICP-MS analyses. This project was funded by the Norwegian University of Science and Technology (NTNU), and the experiments were performed at the Department of Mechanical and Industrial Engineering (MTP).

Conflicts of Interest: The authors declare no conflict of interest.

References

1. Sedriks, A.J. Plenary Lecture—1986: Effects of Alloy Composition and Microstructure on the Passivity of Stainless Steels. *Corrosion* **1986**, *42*, 376–389. [CrossRef]
2. Olsson, C.O.A.; Landolt, D. Passive films on stainless steels—Chemistry, structure and growth. *Electrochim. Acta* **2003**, *48*, 1093–1104. [CrossRef]
3. Newman, R.C. 2001 WR Whitney Award Lecture: Understanding the Corrosion of Stainless Steel. *Corrosion* **2001**, *57*, 1030–1041. [CrossRef]
4. Nilsson, J.O. Super duplex stainless steels. *Mater. Sci. Technol.* **1992**, *8*, 685–700. [CrossRef]
5. Torres, C.; Hazarabedian, M.S.; Quadir, Z.; Johnsen, R.; Iannuzzi, M. The Role of Tungsten on the Phase Transformation Kinetics and its Correlation with the Localized Corrosion Resistance of 25Cr Super Duplex Stainless Steels. *J. Electrochem. Soc.* **2020**, *167*, 081510. [CrossRef]
6. Torres, C.; Johnsen, R.; Iannuzzi, M. Crevice Corrosion of Solution Annealed 25Cr Duplex Stainless Steels: Effect of W on Critical Temperatures. *Corros. Sci.* **2020**. submitted for publication. [CrossRef]
7. Galvele, J.R.; Lumsden, J.B.; Staehle, R.W. Effect of Molybdenum on the Pitting Potential of High Purity 18% Cr Ferritic Stainless Steels. *J. Electrochem. Soc.* **1978**, *125*, 1204. [CrossRef]
8. Newman, R.C.; Ajjawi, M.A.A.; Ezuber, H.; Turgoose, S. An experimental confirmation of the pitting potential model of Galvele. *Corros. Sci.* **1988**, *28*, 471–477. [CrossRef]
9. Suzuki, T.; Yamabe, M.; Kitamura, Y. Composition of Anolyte Within Pit Anode of Austenitic Stainless Steels in Chloride Solution. *Corrosion* **1973**, *29*, 18–22. [CrossRef]
10. Hornus, E.C.; Rodríguez, M.A.; Carranza, R.M.; Rebak, R.B. Comparative Study of the Crevice Corrosion Resistance of UNS S30400 and UNS S31600 Stainless Steels in the Context of Galvele's Model. *Corrosion* **2017**, *73*, 41–52. [CrossRef]
11. Kappes, M.A.; Ortíz, M.R.; Iannuzzi, M.; Carranza, R.M. Use of the Critical Acidification Model to Estimate Critical Localized Corrosion Potentials of Duplex Stainless Steels. *Corrosion* **2017**, *73*, 31–40. [CrossRef]
12. Hornus, E.C.; Giordano, C.M.; Rodriguez, M.A.; Carranza, R.M.; Rebak, R.B. Effect of Temperature on the Crevice Corrosion of Nickel Alloys Containing Chromium and Molybdenum. *J. Electrochem. Soc.* **2015**, *162*, C105–C113. [CrossRef]
13. Galvele, J.R. Transport Processes and the Mechanism of Pitting of Metals. *J. Electrochem. Soc.* **1976**, *123*, 464. [CrossRef]
14. Bocher, F.; Huang, R.; Scully, J.R. Prediction of Critical Crevice Potentials for Ni-Cr-Mo Alloys in Simulated Crevice Solutions as a Function of Molybdenum Content. *Corrosion* **2010**, *66*, 055002-1–055002-15. [CrossRef]
15. Srinivasan, J.; Kelly, R.G. On a Recent Quantitative Framework Examining the Critical Factors for Localized Corrosion and Its Impact on the Galvele Pit Stability Criterion. *Corrosion* **2017**, *73*, 613–633. [CrossRef]
16. Grimm, R.D.; Landolt, D. Salt films formed during mass transport controlled dissolution of iron-chromium alloys in concentrated chloride media. *Corros. Sci.* **1994**, *36*, 1847–1868. [CrossRef]
17. Li, T.; Scully, J.R.; Frankel, G.S. Localized Corrosion: Passive Film Breakdown vs. Pit Growth Stability: Part III. A Unifying Set of Principal Parameters and Criteria for Pit Stabilization and Salt Film Formation. *J. Electrochem. Soc.* **2018**, *165*, C762–C770. [CrossRef]
18. Li, T.; Scully, J.R.; Frankel, G.S. Localized Corrosion: Passive Film Breakdown vs. Pit Growth Stability: Part IV. The Role of Salt Film in Pit Growth: A Mathematical Framework. *J. Electrochem. Soc.* **2019**, *166*, C115–C124. [CrossRef]
19. Statoil ASA. *Technical Note—Metallographic Etching of Duplex Stainless Steels*; Statoil ASA: Oslo, Norway, 2010; MAT–2010080.
20. Robertson, W.D. Molybdate and Tungstate as Corrosion Inhibitors and the Mechanism of Inhibition. *J. Electrochem. Soc.* **1951**, *98*, 94–100. [CrossRef]
21. Alentejano, C.R.; Aoki, I.V. Localized corrosion inhibition of 304 stainless steel in pure water by oxyanions tungstate and molybdate. *Electrochim. Acta* **2004**, *49*, 2779–2785. [CrossRef]
22. Mu, G.; Li, X.; Qu, Q.; Zhou, J. Molybdate and tungstate as corrosion inhibitors for cold rolling steel in hydrochloric acid solution. *Corros. Sci.* **2006**, *48*, 445–459. [CrossRef]
23. Galvele, J.R. Tafel's law in pitting corrosion and crevice corrosion susceptibility. *Corros. Sci.* **2005**, *47*, 3053–3067. [CrossRef]

24. Galvele, J.R. Transport processes in passivity breakdown—II. Full hydrolysis of the metal ions. *Corros. Sci.* **1981**, *21*, 551–579. [CrossRef]
25. Artemov, V.G.; Volkov, A.A.; Sysoev, N.N.; Volkov, A.A. Conductivity of aqueous HCl, NaOH and NaCl solutions: Is water just a substrate? *EPL (Europhys. Lett.)* **2015**, *109*, 26002. [CrossRef]
26. Qvarfort, R. New electrochemical cell for pitting corrosion testing. *Corros. Sci.* **1988**, *28*, 135–140. [CrossRef]
27. Frankel, G.S. *Pitting Corrosion, in Corrosion: Fundamentals, Testing, and Protection*; Cramer, S.D., Covino, B.S., Eds.; ASM International: Cleveland, OH, USA, 2003; pp. 236–241.
28. Henderson, J.D.; Li, X.; Shoesmith, D.W.; Noël, J.J.; Ogle, K. Molybdenum surface enrichment and release during transpassive dissolution of Ni-based alloys. *Corros. Sci.* **2019**, *147*, 32–40. [CrossRef]
29. Salkind, N. *Encyclopedia of Measurement and Statistics*; SAGE Publications: Thousand Oaks, CA, USA, 2007.
30. Pearson, K. Mathematical Contributions to the Theory of Evolution. III. Regression, Heredity, and Panmixia. *Philos. Trans. R. Soc. Lond. Ser. A* **1896**, *187*, 253–318.
31. Croux, C.; Dehon, C. Influence functions of the Spearman and Kendall correlation measures. *Stat. Methods Appl.* **2010**, *19*, 497–515. [CrossRef]
32. Bellezze, T.; Giuliani, G.; Roventi, G. Study of stainless steels corrosion in a strong acid mixture. Part 1: Cyclic potentiodynamic polarization curves examined by means of an analytical method. *Corros. Sci.* **2018**, *130*, 113–125. [CrossRef]
33. Pourbaix, M. *Atlas of Electrochemical Equilibria in Aqueous Solutions*; National Association of Corrosion Engineers (NACE): Houston, TX, USA, 1974.
34. Knyazeva, M.; Pohl, M. Duplex Steels: Part I: Genesis, Formation, Structure, Metallography, Microstructure, and Analysis. *Metall. Microstruct. Anal.* **2013**, *2*, 113–121. [CrossRef]
35. Frankel, G.S. Pitting Corrosion of Metals. *J. Electrochem. Soc.* **1998**, *145*, 2186–2198. [CrossRef]
36. Mankowski, J.; Szklarska-Smialowska, Z. Studies on accumulation of chloride ions in pits growing during anodic polarization. *Corros. Sci.* **1975**, *15*, 493–501. [CrossRef]
37. Srinivasan, J.; McGrath, M.J.; Kelly, R.G. Mass Transport and Electrochemical Phenomena Influencing the Pitting and Repassivation of Stainless Steels in Neutral Chloride Media. *ECS Trans.* **2014**, *58*, 1–11. [CrossRef]
38. Truman, J.E. Stainless Steels. In *Materials Science and Technology*; John Wiley & Sons: Hoboken, NJ, USA, 2006; pp. 529–581. [CrossRef]
39. Bui, N.; Irhzo, A.; Dabosi, F.; Limouzin-Maire, Y. On the mechanism for improved passivation by additions of tungsten to austenitic stainless steels. *Corrosion* **1983**, *39*, 491–496. [CrossRef]
40. Örnek, C.; Leygraf, C.; Pan, J. Passive film characterisation of duplex stainless steel using scanning Kelvin probe force microscopy in combination with electrochemical measurements. *NPJ Mater. Degrad.* **2019**, *3*, 1–8. [CrossRef]
41. Rahimi, E.; Kosari, A.; Hosseinpour, S.; Davoodi, A.; Zandbergen, H.; Mol, J.M.C. Characterization of the passive layer on ferrite and austenite phases of super duplex stainless steel. *Appl. Surf. Sci.* **2019**, *496*, 143634. [CrossRef]
42. Långberg, M.; Örnek, C.; Evertsson, J.; Harlow, G.S.; Linpé, W.; Rullik, L.; Carlà, F.; Felici, R.; Bettini, E.; Kivisäkk, U.; et al. Redefining passivity breakdown of super duplex stainless steel by electrochemical operando synchrotron near surface X-ray analyses. *NPJ Mater. Degrad.* **2019**, *3*, 1–11. [CrossRef]
43. Johnsen, R.; Vingsand, H. Corrosion Properties Of UNS S32750, UNS N06022 And UNS N10276 In Seawater. In Proceedings of the CORROSION 2009, Atlanta, GA, USA, 22–26 March 2009; p. 09195.
44. Haugan, E.B.; Næss, M.; Torres Rodriguez, C.; Johnsen, R.; Iannuzzi, M. Effect of Tungsten on the Pitting and Crevice Corrosion Resistance of Type 25Cr Super Duplex Stainless Steels. *Corrosion* **2017**, *73*, 53–67. [CrossRef]
45. Martínez, P.A.; Hornus, E.C.; Rodríguez, M.A.; Carranza, R.M.; Rebak, R.B. Crevice Corrosion Resistance of Super-Austenitic and Super-Duplex Stainless Steels in Chloride Solutions. In Proceedings of the Corrosion 2015, Dallas, TX, USA, 15–10 March 2015; p. 5740.
46. Deng, B.; Jiang, Y.; Gong, J.; Zhong, C.; Gao, J.; Li, J. Critical pitting and repassivation temperatures for duplex stainless steel in chloride solutions. *Electrochim. Acta* **2008**, *53*, 5220–5225. [CrossRef]
47. Jargelius-Pettersson, R.F.A.; Pires Duarte, B.; Duchamp, G. Pitting Corrosion in Austenitic and Duplex Stainless Steels. *Mater. Sci. Forum* **1998**, *289–292*, 1029–1040. [CrossRef]
48. Machuca, L.L.; Bailey, S.I.; Gubner, R. Systematic study of the corrosion properties of selected high-resistance alloys in natural seawater. *Corros. Sci.* **2012**, *64*, 8–16. [CrossRef]

49. Meng, Q.J.; Adeleke, A.; Derrickson, S. Localized Corrosion Resistance Of UNS S32750 And UNS S33207 Duplex Umbilical Tubes In Synthetic Seawater. In Proceedings of the Corrosion 2010, San Antonio, TX, USA, 14–18 March 2010; p. 10344.
50. Frankel, G.S.; Li, T.; Scully, J.R. Perspective—Localized Corrosion: Passive Film Breakdown vs Pit Growth Stability. *J. Electrochem. Soc.* **2017**, *164*, C180–C181. [CrossRef]
51. Li, T.; Scully, J.R.; Frankel, G.S. Localized Corrosion: Passive Film Breakdown vs Pit Growth Stability: Part II. A Model for Critical Pitting Temperature. *J. Electrochem. Soc.* **2018**, *165*, C484–C491. [CrossRef]